

## Intrinsic charged defects and lithium-ion transport mechanisms in CdPS<sub>3</sub>

Wenqi Xiong<sup>1,2,\*</sup>, Qi Yao<sup>1,3</sup>, and Shengjun Yuan<sup>1,2,†</sup>

<sup>1</sup> Key Laboratory of Artificial Micro- and Nano-structures of the Ministry of Education and School of Physics and Technology, Wuhan University, Wuhan 430072, China

<sup>2</sup> Wuhan Institute of Quantum Technology, Wuhan 430206, China

<sup>3</sup> Quantum Science Centre of Guangdong-Hongkong-Macao Greater Bay Area (Guangdong), Shenzhen 518045, China



(Received 22 August 2023; revised 6 March 2024; accepted 15 March 2024; published 4 April 2024)

Recent studies have unveiled that the electronically insulating CdPS<sub>3</sub> can serve as a versatile solid ion conductor, exhibiting exceptionally high conductivity at room temperature towards various cations. Cd vacancies are believed to play a crucial role in achieving high ionic conductivity, but their specific assisting mechanisms remain unknown. Here, we investigated the synergistic mechanism of Cd-vacancy and Li-ion intercalation using first-principles calculations based on density-functional theory. We found that under a Cd- or P-poor chemical potential, as the Fermi energy approaches the conduction band of CdPS<sub>3</sub>, the formation of Cd vacancies with the  $-1$  charge state  $V_{\text{Cd}}^-$  is energetically favored. The reason for achieving high electrical conductivity is the introduction of a high density of Li ions into Cd vacancies. Keeping the concentration ( $x$ ) of Cd vacancies below 0.5 in Cd<sub>1-x</sub>PS<sub>3</sub>Li<sub>2x</sub> is crucial to ensure high Li-ion conductivity, as concentrations above this threshold lead to a loss of long-range thermal stability and increased energy barriers that impede the diffusion of Li ions. In particular, the Li-ion diffusion barrier in Cd<sub>0.833</sub>PS<sub>3</sub>Li<sub>0.333</sub> is determined to be 0.2 eV, which is highly consistent with the experimental value of  $0.21 \pm 0.022$  eV. Further analysis revealed that Li ions on the surface show a preference for moving along the Cd or S atoms rather than the P atoms. Our research provides insights into the role of vacancies in facilitating cation diffusion, establishing a theoretical framework for the design of high-ionic-conductivity materials.

DOI: 10.1103/PhysRevApplied.21.044011

### I. INTRODUCTION

The rapid transport of ions in nanochannels is crucial in various fields, including energy storage, ion filtration, and life sciences [1–3]. The world is going electric. The first discovery of a solid ionic conductor (SIC) was documented by Faraday in 1833, who reported Ag<sup>+</sup> conduction in Ag<sub>2</sub>S, and later in 1838, F<sup>-</sup> conduction in PbF<sub>2</sub> [4,5]. With the increasing prevalence of mobile devices and smart products, the research focus has shifted to SICs capable of conducting various ions (such as Li<sup>+</sup>, Na<sup>+</sup>, Mg<sup>2+</sup>, and Al<sup>3+</sup>) in nanochannels [6,7]. However, the conductivity of ions is generally lower than  $10^{-3}$  S cm<sup>-1</sup> at room temperature due to the steric effect and Coulomb interaction with the channel walls [6–8]. In addition, the ion conductivity decreases with temperature [6,9]. To date, few SIC materials have demonstrated effective ion conductivity ( $>0.01$  S cm<sup>-1</sup>) below 0 °C.

Following transition metal dichalcogenides and black phosphorus [10,11], transition metal phosphorus trichalcogenides ( $MPX_3$ ,  $M = \text{Cd, Zn, Mn, Mg, Co}$ , etc;  $X = \text{S, Se}$ ) have emerged as a prominent research hotspot in the field of two-dimensional (2D) materials due to their superconducting [12], catalytic [13,14], and optoelectronic properties [15,16]. Recently, ZnPS<sub>3</sub> has been reported as the first electronically insulating SIC capable of enabling Zn<sup>2+</sup> conduction with a Li<sup>+</sup> activation energy of  $351 \pm 99$  meV. However, its ionic conductivity at 60 °C remains extremely low, at approximately  $10^{-7}$  S cm<sup>-1</sup> [17]. Furthermore, recent studies have found that artificially introduced vacancies can enhance the ionic conduction performance. Qian *et al.* reported the synthesis of CdPS<sub>3</sub> crystals by the chemical vapor transport method, where Cd vacancies were created by alkaline ion exchange [18]. The 2D Cd<sub>0.85</sub>PS<sub>3</sub>Li<sub>0.3</sub> membranes showed superior Li-ion conductivity, 3 to 5 orders of magnitude higher than metal organic framework membranes [19]. Later, Yang *et al.* found that the synergistic effect of Li ions and Cd vacancies accelerates ion transport in 2D Cd<sub>1-x</sub>PS<sub>3</sub>Li<sub>2x</sub> nanosheets, enabling them to be used as anodes for

\*Corresponding authors: wqxiong@whu.edu.cn

†s.yuan@whu.edu.cn

high-capacity lithium-ion batteries [20]. Yu and Ren discovered that monolayer CdPS<sub>3</sub> could act as a multi-functional SIC, exhibiting remarkably high conductivity for various cations (K<sup>+</sup>, Na<sup>+</sup>, Li<sup>+</sup>, Ca<sup>2+</sup>, Mg<sup>2+</sup>, Al<sup>3+</sup>), ranging from 0.01 to 0.8 S cm<sup>-1</sup> within the temperature range of -30 to 90 °C [21]. These studies suggest that Cd vacancies have been an effective means to enhance the conductivity of 2D CdPS<sub>3</sub>; however, the cause of Cd vacancies and the mechanism of Li-ion diffusion assisted by Cd defects have not been investigated yet.

In this work, our aim was to study the formation energy and charge transition levels of various defects in 2D CdPS<sub>3</sub> using three exchange-correlation (XC) functionals. We found that Cd vacancies are the dominant native defects in a highly electron-rich environment. We also used the climbing-image nudged elastic band (CINEB) algorithm to calculate the diffusion paths and migration barriers of Li ions assisted by Cd vacancies in a Cd<sub>1-x</sub>PS<sub>3</sub>Li<sub>2x</sub> membrane (where  $x$  is the Cd-vacancy concentration) [22,23]. Furthermore, we investigated the effects of Cd-vacancy or Li-ion concentration on the thermodynamic and chemical stability of the Cd<sub>1-x</sub>PS<sub>3</sub>Li<sub>2x</sub> membrane. Subsequently, we aimed to optimize the diffusion barriers and pathways for Li ions and corroborate our results with experimental observations. Finally, we combined the intrinsic defect concentration and Li-ion diffusion rate to obtain experimentally comparable Li-ion conductivity.

## II. METHODS

The density-functional theory (DFT) calculations presented in this paper were performed using the VASP package [24–26]. The projector-augmented wave potentials with valence electron configurations of 4d<sup>10</sup>5s<sup>2</sup>, 3s<sup>2</sup>3p<sup>3</sup>, 3s<sup>2</sup>3p<sup>4</sup>, and 2s<sup>1</sup> were used to model Cd, P, S, and Li, respectively [27]. As structural optimization, electronic structure, and thermodynamic transition levels are interrelated with the XC functional, their descriptions are provided by Perdew-Burke-Ernzerhof (PBE), strongly constrained and appropriately normed (SCAN) meta-generalized gradient approximation (meta-GGA), and Heyd-Scuseria-Ernzerhof (HSE06) functionals [28–30]. These XC functionals are generally ranked in terms of accuracy and computational cost as PBE < SCAN < HSE06. For the spin polarization calculations, the cutoff energy of the plane-wave basis and the Monkhorst-Pack mesh were set to 350 eV and 15 × 15 × 1, respectively [31]. The stress force and energy convergence criteria were set to 0.01 eV/Å and 10<sup>-5</sup> eV, respectively. The vacuum region of 20 Å was used to avoid the periodic interaction. The long-range van der Waals (vdW) interaction was included using the semiempirical DFT-D2 and SCAN-rVV10 methods [32,33]. The spin-orbit coupling (SOC) effect was included in the self-consistent calculations. All atoms were allowed to be fully optimized to

the ground state. We modeled the defective systems by constructing a 3 × 3 × 1 CdPS<sub>3</sub> supercell.

The thermodynamic stability of Li-doped CdPS<sub>3</sub> was checked by performing *ab initio* molecular dynamics (AIMD) simulations in a canonical ensemble (*NVT*) at 300 K with a 5 ps duration [34,35]. Furthermore, the post-processing of the AIMD simulation data was also done using the VASPKIT program [36].

To investigate the Li-ion diffusion process, we utilized the CINEB approach implemented in VASP (VASP VTST) to search for the minimum energy path (MEP) profiles [22,23]. The diffusion barrier was defined as the energy difference between the initial state (IS) and the transition state (TS). To ensure the accuracy of the MEP search, the convergence criteria of the spring force was set to 0.05 eV/Å.

## III. RESULTS AND DISCUSSION

### A. Fundamental properties of perfect crystals

Single-layer CdPS<sub>3</sub> exhibits a hexagonal lattice structure with a space group of  $P\bar{3}1m$ , which is obtained by exfoliating the bulk structure composed of ABC-stacked vdW multilayers [37,38]. The unit cell consists of two Cd atoms, two P atoms, and six S atoms [Fig. 1(a)]. In the CdPS<sub>3</sub> structure, [P<sub>2</sub>S<sub>6</sub>]<sup>4-</sup> anions are arranged bilaterally in a triangular sublattice, creating hole nests for Cd cations. This unique arrangement allows reversible migration of Cd<sup>2+</sup> ions without the need for structural reconstruction. The geometric structure was fully optimized using three XC functionals, and the lattice and structural parameters are presented in Table S1 in the Supplemental Material [39]. It is worth noting that the PBE functional tends to overestimate the lattice constants and bond lengths, a known problem referred to as supertetragonality [40]. On the other hand, the HSE06 functional yields the parameters that are closest to the experimental values of bulk compounds [41].

In Fig. 1(d), the DFT band structures show that the valence band minimum (VBM) emerges at the  $K$  point, while the conduction band maximum (CBM) is located at the  $\Gamma$  point, resulting in an indirect band structure. The PBE and SCAN functionals yield the band-gap values of 1.92 and 2.44 eV, respectively. Applying the HSE06 functional for correction, the band-gap value increases to 3.12 eV. Although there are no experimental reports on the optical band-gap values of single-layer or few-layer CdPS<sub>3</sub>, the band gap of 2D CdPS<sub>3</sub> is slightly larger than its bulk counterpart due to quantum confinement effects. Therefore, the HSE06 functional provides the most accurate band-gap value [42]. It is important to note that the defect formation energy is closely related to the band-gap value. However, PBE and SCAN functionals tend to underestimate the band gaps of semiconductors. As a

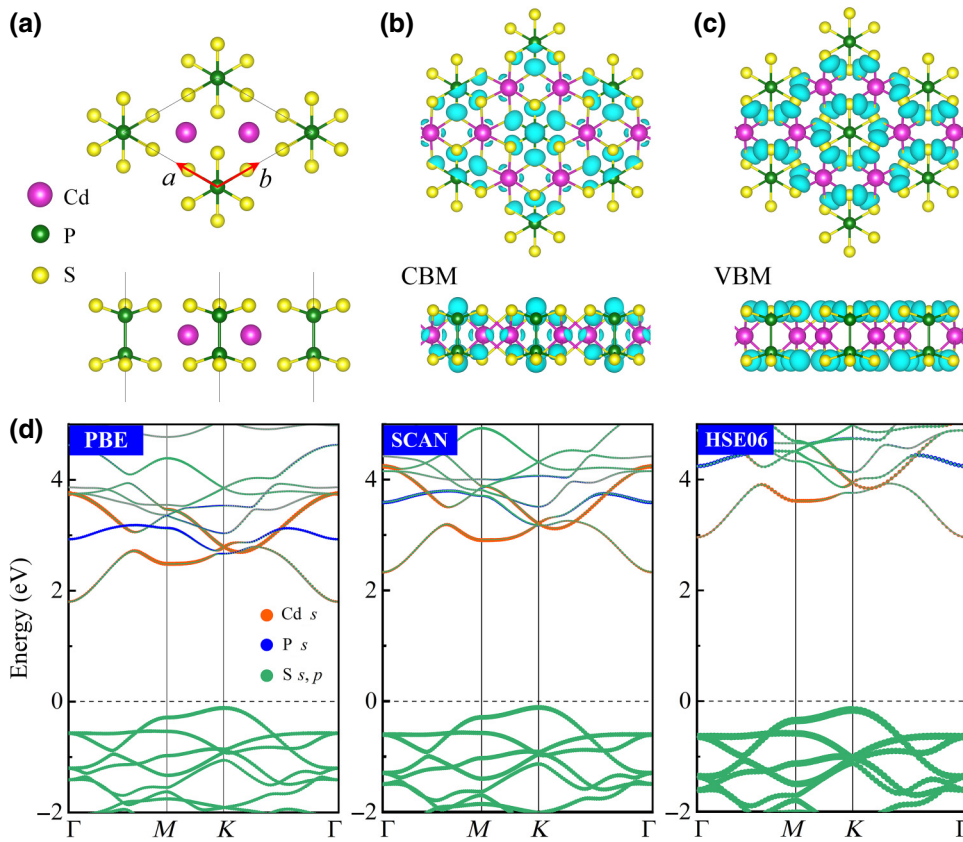


FIG. 1. (a) Top and side views of CdPS<sub>3</sub> unit cell. (b) Band-decomposed charge density for conduction band maximum (CBM) (b) and valence band minimum (VBM) (c) of CdPS<sub>3</sub>. (d) Projected band structures of CdPS<sub>3</sub> using the PBE, SCAN, and HSE06 functionals. The Fermi level is set to zero.

result, the HSE06 functional is generally considered more appropriate for these calculations [43].

The band-decomposed charge densities depicted in Figs. 1(b) and 1(c) indicate that the CBM states are distributed among the Cd, P, and S atoms, while the VBM states are mainly concentrated around the S atoms. To further analyze the orbital contributions, we calculated the projected band structures and projected them onto the atomic orbitals of the Cd, P, and S atoms, as shown in Fig. 1(d). We found that the VBM states are mainly derived from the *p<sub>x</sub>* and *p<sub>y</sub>* orbitals of S atoms, whereas the CBM states are derived from the overlap of Cd *s*, P *s*, S *s*, and S *p<sub>z</sub>* orbitals. Furthermore, in Fig. S1 in the Supplemental Material [39], we observe a complete overlap in the band structures of SCAN (PBE) calculations with and without consideration of the SOC effect, indicating that the SOC effect does not modify the band dispersion. Therefore, we neglect the SOC effect in the following sections.

## B. Defect formation energies

The formation energy  $E_f[X^q]$  of a point defect  $X$  with different charge states  $q$  using a supercell approach is

defined as follows [44,45]:

$$E_f[X^q] = E_{\text{tot}}[X^q] - E_{\text{tot}}[\text{host}] - \sum n_i \mu_i + q \varepsilon_e + E_{\text{corr}}, \quad (1)$$

where  $E_{\text{tot}}[X^q]$  and  $E_{\text{tot}}[\text{host}]$  are the total energies of 2D CdPS<sub>3</sub> with and without the charged defect  $X^q$ , respectively. The integer  $n_i$  represents the number of atoms *i* added to ( $n_i > 0$ ) or deleted from ( $n_i < 0$ ) host structures.  $\mu_i$  is the chemical potential of a reservoir of atoms *i* and is given by  $\mu_i^0 + \Delta\mu_i$ .  $\Delta\mu_i$  is defined with respect to the chemical potential of element *i* in its ground state  $\mu_i^0$ .  $\varepsilon_e = \varepsilon_F + \varepsilon_v$  denotes the Fermi energy, ranging from CBM to VBM, so  $\varepsilon_v$  is the energy of the VBM and  $\varepsilon_F$  is the Fermi level with respect to the VBM.  $E_{\text{corr}}$  is the correction term that contains the electrostatic interactions of charged defects on the finite-size supercell and the compensating background charge [46,47]. Here, we treated the correction term  $E_{\text{corr}}$  using the Freysoldt-Neugebauer correction scheme [44,46]. A detailed explanation can be found in the Supplemental Material [39].

Figure 2 plots the chemical potential diagrams of CdPS<sub>3</sub> obtained from the PBE, SCAN, and HSE06 functionals used to determine the defect formation energies [Eq.

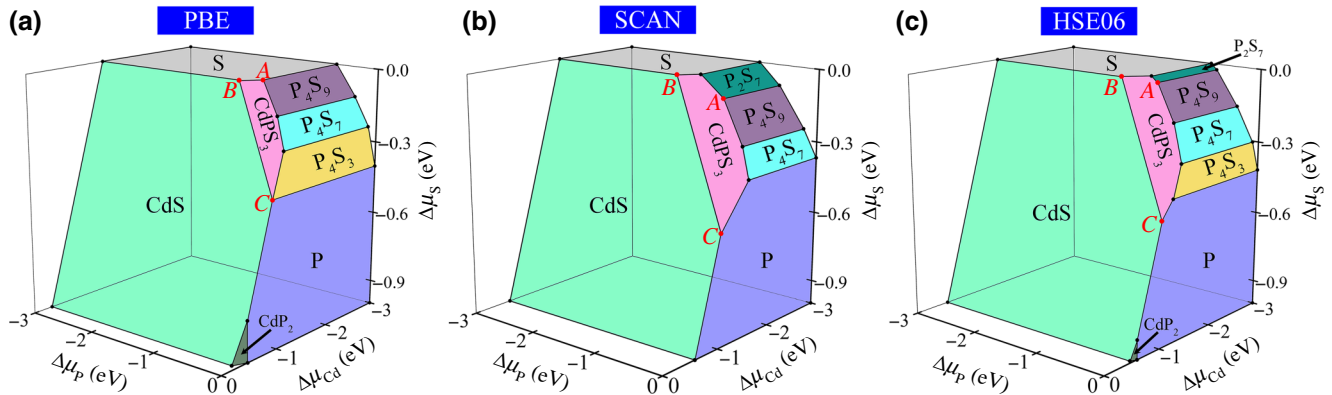


FIG. 2. The calculated chemical potentials  $\Delta\mu_i$  with respect to the ground state of 2D CdPS<sub>3</sub> from PBE (a), SCAN (b), and HSE06 (c) functionals. By preventing the formation of various secondary phases, the purple regions represent the conditions that allow for the synthesis of CdPS<sub>3</sub>. Labels A, B, and C correspond to Cd-poor, P-poor, and S-poor conditions, respectively, which are deemed as extreme cases.

(1)]. Table S2 in the Supplemental Material lists various secondary compounds that must be constrained in the phase diagram [39]. The relative chemical potentials  $\Delta\mu_i$  for Cd-poor, P-poor, and S-poor conditions from different functionals are listed in Table S3 in the Supplemental Material [39]. From Fig. 2, it is clear that the growth of stable single-phase CdPS<sub>3</sub> is limited to a narrow region (highlighted by the purple region). The chemical potentials are affected by the experimental conditions and can be controlled by appropriate setups. As a result, differences in the chemical potential cause changes in the defect formation energy.

In the present study, we investigated seven different native point defects, including three monovacancies ( $V_{Cd}$ ,  $V_p$ , and  $V_S$ ) and four divacancies ( $V_{Cd2}$ ,  $V_{P2}$ ,  $V_{1S2}$ , and  $V_{2S2}$ ), as depicted in Fig. S2 in the Supplemental Material [39]. We calculated their defect formation energies  $E_f[X^q]$  under three different growth conditions (Cd-, P-, and S-poor) and considered their possible charged states ( $q = 0, \pm 1$ ). The results are plotted as a function of Fermi energy  $\varepsilon_F$  in Fig. 3. The charge transition levels for each defect are summarized in Table I.

To verify the convergence of the defect formation energy, we calculated the formation energy of the Cd vacancy under different supercell sizes. Table S4 in the Supplemental Material [39] indicates that the changes in formation energy for the neutral Cd vacancy under different sizes is less than 0.1 eV. Considering charged Cd vacancies ( $q = \pm 1$ ), the defect formation energy in the  $3 \times 3$  supercell is similar to that in the larger  $4 \times 4$  supercell, with a difference of about 0.1 eV. This shows that the  $3 \times 3$  supercell used for defect calculations is reliable.

As depicted in Fig. 3, among the neutral charge states, the S vacancy  $V_S$  is the dominant defect and does not undergo any charge state transition, indicating that it cannot act as an acceptor or donor defect. Among the S

divacancies,  $V_{1S2}$  is found to be more stable than  $V_{2S2}$ .  $V_{1S2}$  does not experience any charge state transition, while the (+/0) charge transition of  $V_{2S2}$  occurs within the band gap near the VBM. For the P vacancy  $V_p$ , the PBE and SCAN results show that the (+/0) charge transition occurs at 0.72 eV and 0.82 eV above VBM. The (0/-) charge transition is only observed in the HSE06 results due to the underestimation of the band gaps by PBE and SCAN.  $V_{Cd}$  acts as a deep electron trap center and the transition level of  $\varepsilon(0/-)$  occurs at 0.83, 1.00, and 1.03 eV above VBM for PBE, SCAN, and HSE06 functionals. In addition, when more accurate XC functionals (SCAN and HSE06) with improved correction are applied, higher defect formation energies are obtained compared to PBE, in agreement with the results of previous studies [48,49].

We have also investigated the effect of the chemical potential on the formation of these native defects. When the host material is *p* type, the neutral S vacancy  $V_S^0$  remains dominant (Fig. 3). However, in an electron-rich environment, such as under Cd- or P-poor conditions, the charged Cd vacancy  $V_{Cd}^-$  becomes more stable and dominates for  $\varepsilon_F > 1.46$ , 1.46, and 2.26 eV in PBE, SCAN, and HSE06 functionals. Other charge state tests indicate that  $V_{Cd}^-$  remains the most stable among all charge states when the Fermi level approaches the CBM (see Fig. S3 in the Supplemental Material [39]). Therefore, avoiding an S-poor condition can enhance the concentration of Cd vacancies in CdPS<sub>3</sub>. For the synthesis of CdPS<sub>3</sub> nanosheets, the use of chemical vapor deposition or chemical vapor transport methods in an electron-rich environment with Cd- or P-poor conditions are recommended to generate a charged Cd vacancy  $V_{Cd}^-$ . This suggestion is supported by the HSE06 results, which indicate that the formation energy of charged Cd vacancies approaches zero as  $\varepsilon_F$  moves to the CBM, resulting in even higher concentrations of Cd vacancies.

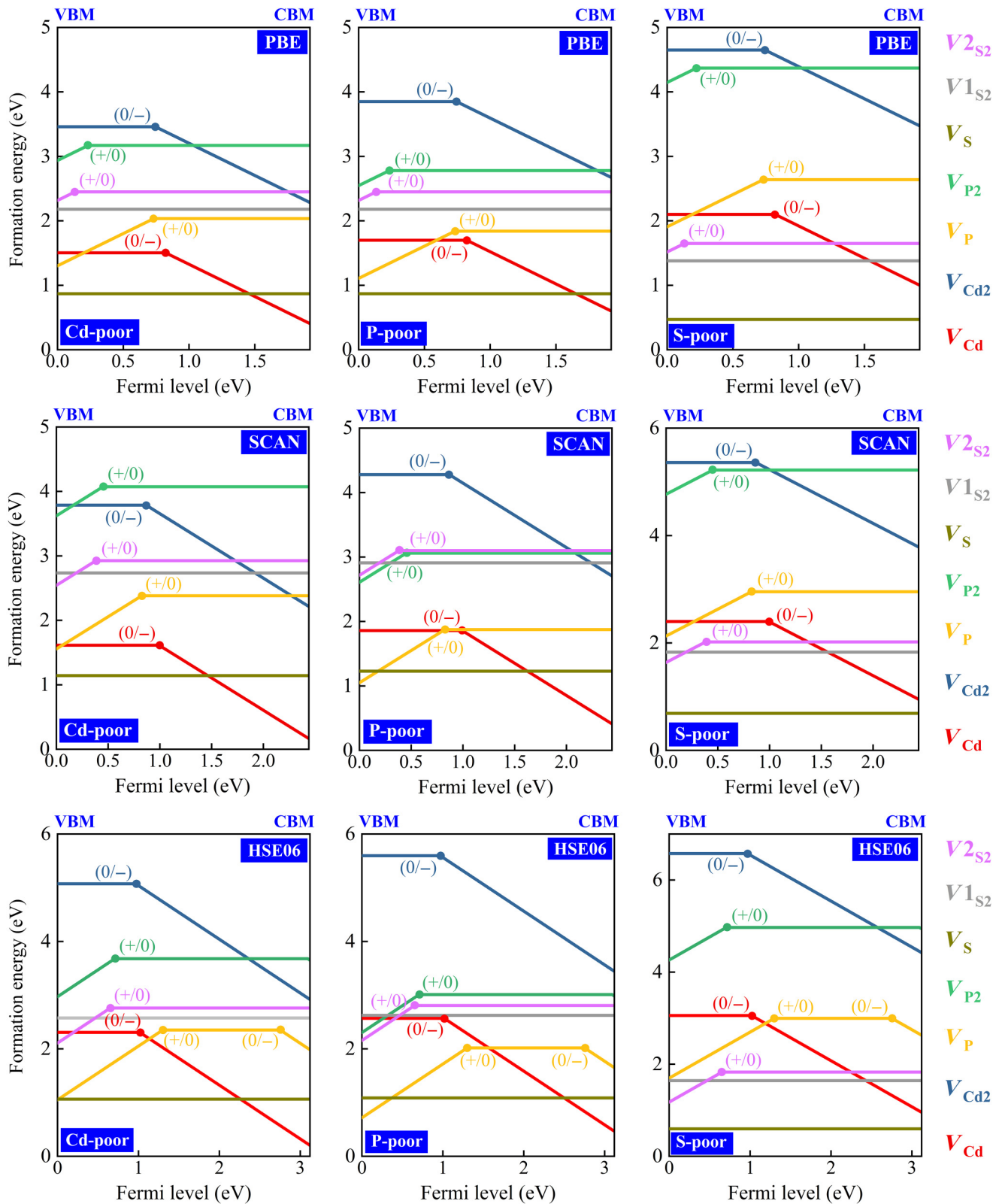


FIG. 3. Defect formation energies of the charged point defects in  $\text{CdPS}_3$  under the Cd-poor, P-poor, and S-poor growth conditions as a function of Fermi level calculated with the PBE, SCAN, and HSE06 functionals. The Fermi level shifts from VBM to CBM.

TABLE I. Calculated positions of the charge transition level (in eV)  $\epsilon(+/-)$  and  $\epsilon(0/-)$  with respect to VBM. The minus sign (-) denotes that the charge transition levels do not lie in the band gap of the host material. The transition level is independent of the chemical potential.

	$V_{\text{Cd}}$	$V_{\text{Cd}2}$	$V_{\text{P}}$	$V_{\text{P}2}$	$V_{\text{S}}$	$V_{1\text{S}2}$	$V_{2\text{S}2}$
PBE	0.83	0.74	0.72	0.23	—	—	0.13
SCAN	1.00	0.87	0.82	0.45	—	—	0.38
HSE06	1.03	0.97	1.31, 2.76	0.71	—	—	0.65

We then focus on discussing the short-range interaction between two isolated monovacancies in CdPS<sub>3</sub>. For this purpose, we created two Cd vacancies at a distance of 3.6–10.8 Å in a nanosheet [Fig. S4(a) in the Supplemental Material] [39]. The relative formation energies of the charged Cd divacancy  $V_{\text{Cd}2}^-$  are plotted as a function of the distance  $L$  in Fig. S4(b) in the Supplemental Material [39]. The formation energy increases linearly with decreasing distance, indicating Coulomb repulsion between charged vacancies. The electrostatic interaction energy  $\Delta E$  between images of charge  $q$  is expressed as  $\Delta E \sim q^2/2\varepsilon L$  [50,51], where  $\varepsilon$  is the dielectric constant and  $L$  is the divacancy distance. The larger the distance between charged defects, the smaller the electrostatic interaction energy. Ohwada *et al.* observed that the concentration of Ti divacancies on TiO<sub>2</sub> nanosheets was much lower than that of monovacancies, suggesting a similar electrostatic repulsion interaction [52]. Interestingly, the distance of the S divacancy in  $V_{1\text{S}2}$  (3.93 Å) is larger than that in  $V_{2\text{S}2}$  (3.39 Å), which may explain why the defect formation energy of  $V_{1\text{S}2}$  is lower than that of  $V_{2\text{S}2}$  in Fig. 3.

Figure 4 illustrates the projected density of states (DOS) for CdPS<sub>3</sub> without defects and for the negatively charged Cd vacancy with a -1 charge state ( $V_{\text{Cd}}^-$ ) along the charge isosurfaces of the relevant states. In Fig. 4(a), the CBM states are composed of Cd, P, and S atoms, while the VBM mainly arises from S atoms. The real-space charge density of peak A appears to be uniformly distributed around the S atoms [Fig. 4(c)]. The formation of a Cd vacancy in CdPS<sub>3</sub> results in the appearance of midgap defect states (peak B) at the Fermi level, which are mainly caused by the surrounding S atoms [Fig. 4(b)]. Additionally, the charge density distributions of peak B at the Fermi level exhibit a triangular shape centered around the Cd vacancy [Fig. 4(d)]. When excess electrons are added to the Cd vacancy, unpaired electrons localize around the surrounding S atoms to form new occupied states at the Fermi level.

### C. Chemical and thermal stability

Since single-layer CdPS<sub>3</sub> exhibits high Li-ion conductivity with the assistance of Cd defects [18,20], we studied

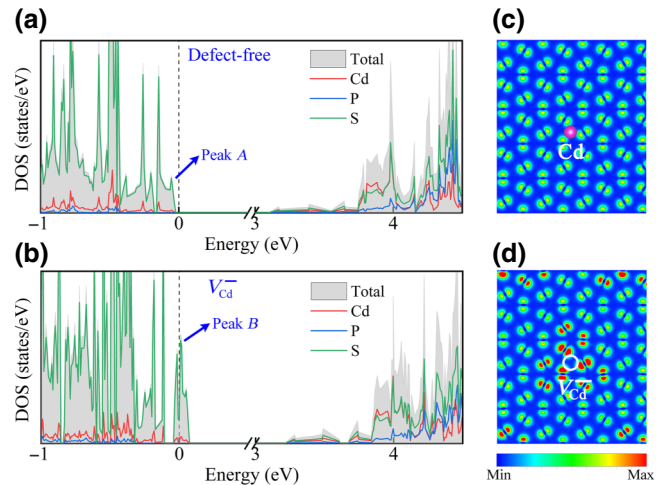


FIG. 4. Projected density of states (DOS) for 2D CdPS<sub>3</sub> (a) without defects and (b) with Cd vacancies ( $V_{\text{Cd}}^-$ ) calculated with the HSE06 functional. Total DOS is displayed in gray shadow. The dashed line indicates the Fermi level. Charge densities for peak A (c) and peak B (d) in DOS. The positions of Cd atom and corresponding Cd vacancy ( $V_{\text{Cd}}^-$ ) are marked.

the diffusion reaction between Li ions and Cd vacancies. As shown in Fig. 5(a), to compensate for the high charge of Cd<sup>2+</sup>, two Li<sup>+</sup> ions are likely to occupy one Cd<sup>2+</sup> site of Cd<sub>1-x</sub>PS<sub>3</sub>Li<sub>2x</sub> [18]. As the Cd vacancies are saturated with Li<sup>+</sup>, the Li<sup>+</sup>-doping concentration (2x) is twice the  $V_{\text{Cd}}$  concentration ( $x$ ) in the Cd<sub>1-x</sub>PS<sub>3</sub>Li<sub>2x</sub> compound. To evaluate the chemical stability of the Cd<sub>1-x</sub>PS<sub>3</sub>Li<sub>2x</sub> compound [53], the formation enthalpy ( $\Delta H$ ) is given by the following equation:  $\Delta G = \Delta H - T\Delta S$ , where  $\Delta G$  is the Gibbs free energy change and  $\Delta S$  is the entropy. Since the temperature in DFT calculations is  $T=0$  K,  $T\Delta S$  is equal to zero, i.e.,  $\Delta G = \Delta H$ . Hence, the formation enthalpy  $\Delta H$  of Cd<sub>1-x</sub>PS<sub>3</sub>Li<sub>2x</sub> can be proposed as follows:

$$\Delta H = E_{\text{Cd}_{1-x}\text{PS}_3\text{Li}_{2x}} - E_{\text{CdPS}_3} - 2xE_{\text{Li}} + xE_{\text{Cd}}, \quad (2)$$

where  $E_{\text{Cd}_{1-x}\text{PS}_3\text{Li}_{2x}}$  and  $E_{\text{CdPS}_3}$  are the total energies of the Cd<sub>1-x</sub>PS<sub>3</sub>Li<sub>2x</sub> compound and pristine CdPS<sub>3</sub>.  $E_{\text{Li}}$  and  $E_{\text{Cd}}$  are the total energies per atom in their bulk phases. Figure 5(b) provides the formation enthalpy  $\Delta H$  of the Cd<sub>1-x</sub>PS<sub>3</sub>Li<sub>2x</sub> nanosheet as a function of Cd-vacancy concentration  $x$ . It can be observed that the formation enthalpy shows a linear relationship with the concentration  $x$ . As the Li-ion concentration increases, the formation enthalpy becomes more negative and the chemical stability increases. This is mainly because the bond energy of Li—S (2.72 eV) is almost twice that of Cd—S (1.33 eV), suggesting that Li ions tend to be introduced at the Cd defects in CdPS<sub>3</sub>.

Next, to investigate the thermodynamic stability of the Cd<sub>1-x</sub>PS<sub>3</sub>Li<sub>2x</sub> compound at room temperature (300 K), we performed AIMD simulations by heating it in the *NVT*

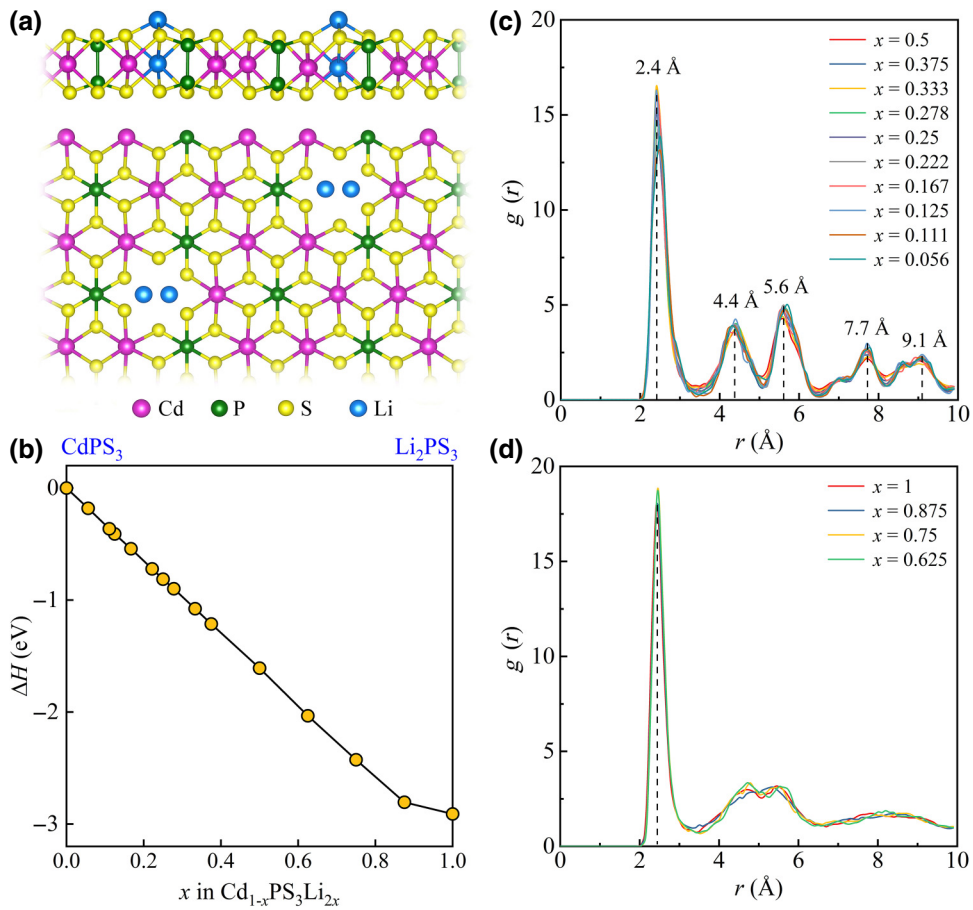


FIG. 5. (a) The side and top views of  $\text{Cd}_{1-x}\text{PS}_3\text{Li}_{2x}$ . (b) Corresponding formation enthalpy ( $\Delta H$ ) as a function of the Cd-vacancy concentration  $x$ . (c)–(d) The radius distribution function [ $g(r)$ ] of  $\text{Cd}_{1-x}\text{PS}_3\text{Li}_{2x}$  at 300 K for different Cd-vacancy concentrations  $x$ .

ensemble for 5 ps. Figure S5 in the Supplemental Material [39] shows the postsimulation structures, revealing that  $\text{Cd}_{1-x}\text{PS}_3\text{Li}_{2x}$  undergoes large structural distortions when the concentration  $x$  exceeds 0.5, leading to the disruption of its  $[\text{P}_2\text{S}_6]^{4-}$  anions in the triangular sublattice [39]. Figures 5(c) and 5(d) show the radius distribution function for the Li—S bond in  $\text{Cd}_{1-x}\text{PS}_3\text{Li}_{2x}$  at 300 K as a function of radius ( $r$ ). The first peak at a radius of 2.4 Å corresponds to the Li—S bond, while the following four peaks correspond to the neighboring Li—S distances. In particular, when  $x \leq 0.5$ , all five peaks show consistently sharp profiles. In contrast, when  $x > 0.5$ , the last four peaks are broadened. This indicates that the  $\text{Cd}_{1-x}\text{PS}_3\text{Li}_{2x}$  compound can only maintain long-range thermal stability at concentrations  $x \leq 0.5$ .

#### D. Diffusion barriers

To determine the Li-ion diffusion pathway, we moved the Li ion outside the Cd vacancy to a neighboring equivalent vacancy. Figure S6 in the Supplemental Material [39] shows the migration paths of Li ions at different

concentrations  $x$ , and Fig. S7 in the Supplemental Material [39] collects the total energy variation along the entire migration paths using the PBE + CINEB tool [39]. Figure 6 shows the distribution of the Li-ion diffusion barrier at different concentrations  $x$ . It can be observed that when  $x \leq 0.5$ , the Li-ion diffusion barrier  $E_b$  remains in the range 0.2–0.3 eV, which is due to the preservation of the long-range structural stability. The experimentally reported Li-ion diffusion barrier of  $0.21 \pm 0.022$  eV in  $\text{Cd}_{0.85}\text{PS}_3\text{Li}_{0.3}$  membranes by Qian *et al.* falls within our predicted range [18]. Previous reports have also shown that the increased concentration of Li ions contributes to the high density of cations in the well-ordered nanochannels, leading to higher electrical conductivity in the electrode conductors [21,54]. However, when  $x > 0.5$ , the disruption of the structural stability leads to a rapid increase in the diffusion barriers, hindering the transport of the Li ions. From the perspective of structural stability and diffusivity, to achieve high Li-ion conductivity in  $\text{CdPS}_3$ , the concentration of Li-ion doping on Cd vacancies ( $x$ ) should be less than 0.5.

Here we provide a simple explanation for the minimum diffusion barrier of Li ions at  $x = 0.166$ . The diffusion barriers of Li ions on  $\text{CdPS}_3$  are mainly determined by the

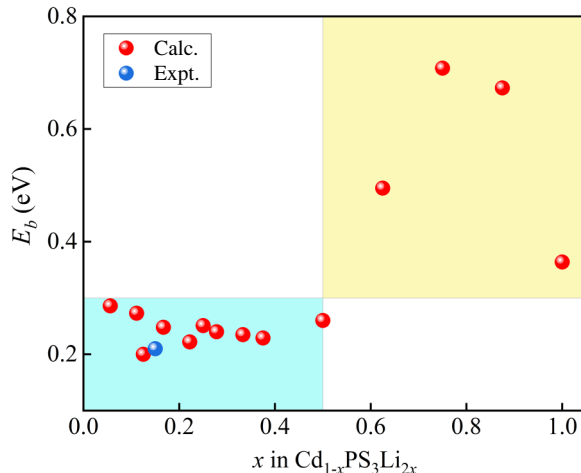


FIG. 6. Calculated Li-ion diffusion barrier  $E_b$  via PBE on  $\text{Cd}_{1-x}\text{PS}_3\text{Li}_{2x}$  for different concentrations  $x$ . Red symbols denote calculated data at different  $x$ ; blue symbols denote experimental data from Ref. [18].

interaction between Li ions and surface sites, as well as the structural symmetry. The doping of Li ions in  $\text{CdPS}_3$  can influence the symmetry of the local structure. Since the maximum energy along the Li-ion diffusion pathway occurs at the Cd atomic site [see Fig. 7(b)], we measured the distances between adjacent S atoms in the  $[\text{CdS}_6]^{4-}$  anion, as shown in Ref. [39]. The results indicate that when  $x = 0.166$ , the incorporation of Li ions has the least effect on the local symmetry around Cd, making it the most favorable for Li-ion diffusion.

To ensure an accurate comparison with the Li-ion diffusion barrier on  $\text{Cd}_{0.85}\text{PS}_3\text{Li}_{0.3}$ , as investigated by Qian *et al.* [18], we also employed the PBE, SCAN, and HSE06 functionals to investigate the Li-ion diffusion reactions on a  $\text{Cd}_{0.833}\text{PS}_3\text{Li}_{0.333}$  sample. As shown in Fig. 7(a), when two Li ions occupy the Cd vacancy, one of the Li ions replaces the original Cd atom to form a stable bonding structure that is virtually immobile. The other Li ion adsorbed on the surface position is weakly bound and can undergo ion exchange. In Fig. 7(a), we have attempted two possible pathways for surface Li-ion migration: path I follows the movement of the P and S atoms, whereas path II follows that of the Cd and S atoms. The entire diffusion process is negatively charged ( $q = -1$ ). Figure 7(b) shows the evolution of the total energy as the Li ion moves, and Table II summarizes the numerical values of the energy barriers. The diffusion barrier of Li ions along path I is much lower than that along path II, indicating that Li ions preferentially move along Cd and S atoms rather than P and S atoms. In Figs. 7(c)–7(e), to elucidate the underlying reasons contributing to the preferential migration pathway, we have calculated the charge density difference to evaluate the charge coupling between Li ions and  $\text{CdPS}_3$ . Combined with the Bader charge analysis [55], it was found that the

Li ion and the Cd and P atoms lose charge (cyan region) while the S atoms gain charge (red region). In Figs. 7(c) and 7(e), when the Li ion is placed above Cd or S atoms, the positive Li ion is attracted to the negative Cd or S atom, and the shorter Li–S bond indicates that the structures are energetically stable. In Fig. 7(d), when the Li ion is located above P atoms, it experiences repulsion from the positively charged P atoms, causing it to move away from the surface. This suggests that the Li-ion diffusion pathway cannot involve the P atoms.

Furthermore, Table II shows that the diffusion barrier calculated using the SCAN functional is overestimated by about 10–100 meV compared to PBE and HSE06. Among these functionals, HSE06 gives the lowest energy barrier  $E_b$  of 0.213 eV for path I. The highest energy point, also known as TS, of the Li-ion migration occurs on the Cd atom near IS. Based on the harmonic transition state theory, we estimated the activation energy  $E_a$  taking into account the zero-point energy (ZPE) correction,

$$E_a = E_b + \frac{1}{2} \sum_{i=1}^{3N-1} h\omega_i^{\text{TS}} - \frac{1}{2} \sum_{i=1}^{3N} h\omega_i^{\text{IS}}, \quad (3)$$

where  $h$  is the Planck constant, and  $\omega_i^{\text{TS}}$  and  $\omega_i^{\text{IS}}$  are the vibrational frequencies of the  $i$ th mode in the TS and IS, respectively. The ZPE correction value is about 15 meV. After accounting for the ZPE correction, the activation barrier  $E_a$  for Li-ion diffusion along path I obtained by HSE06 is 0.2 eV, which is highly consistent with the experimentally measured barrier of  $0.21 \pm 0.022$  eV in  $\text{Cd}_{0.85}\text{PS}_3\text{Li}_{0.3}$  membranes [18]. However, the results obtained by PBE and SCAN overestimate the activation barriers for Li-ion diffusion.

The calculated diffusion barriers can be used to estimate the diffusion rate  $\Gamma$ ,

$$\Gamma = \Gamma_0 \exp\left(-\frac{E_a}{k_B T}\right), \quad (4)$$

where  $k_B$  is the Boltzmann constant and  $T$  is the temperature. The preexponential factor  $\Gamma_0$  is expressed as follows [56]:

$$\Gamma_0 = \frac{k_B T}{h} \frac{\prod_{i=1}^{3N} (1 - \exp(-(h\omega_i^{\text{IS}}/k_B T)))}{\prod_{i=1}^{3N-1} (1 - \exp(-(h\omega_i^{\text{TS}}/k_B T)))}. \quad (5)$$

In Fig. S9 in the Supplemental Material [39], the diffusion rate  $\Gamma$  for the Li ion is plotted as a function of temperature  $T$  in the range 200–500 K, and it is inversely proportional to temperature ( $1/T$ ) [39]. Since the diffusion rate  $\Gamma$  depends exponentially on the activation barrier  $E_a$ , the diffusion rates of Li ions along path I are 7–12 orders of magnitude higher than those along path II. At room temperature (300 K), the diffusion rates of Li ions along path I obtained by PBE, SCAN, and HSE06 are  $5.22 \times 10^8$ ,

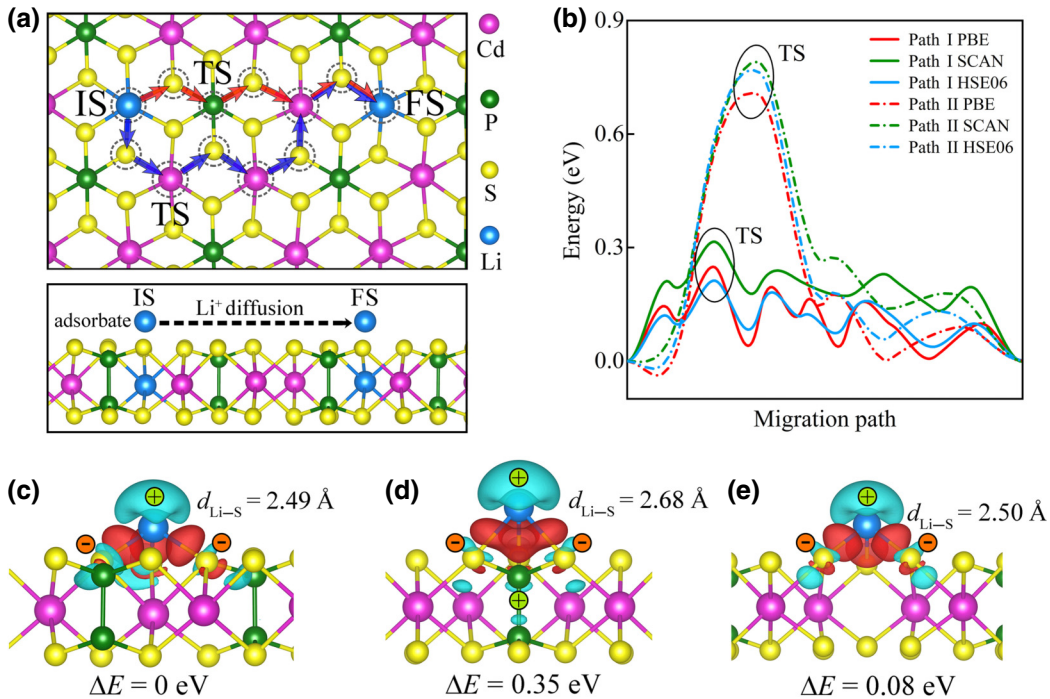


FIG. 7. Li-ion diffusion on Cd<sub>0.833</sub>PS<sub>3</sub>Li<sub>0.333</sub>: diffusion paths from initial state (IS) to final state (FS) (blue, path I; red, path II) (a) and corresponding energy profiles at transition state (TS) (b). The charge density difference for Li-ion adsorption above Cd (c), P (d), and S (e) atoms. Red and cyan clouds represent charge accumulation and depletion. The Li—S bond lengths, atomic charges, and relative energies are represented in (c)–(e).

$4.09 \times 10^7$ , and  $2.05 \times 10^9$  s<sup>-1</sup>. These values show that the mobility of Li ions on CdPS<sub>3</sub> with Cd vacancies is exceptionally high.

### E. Lithium-ion conductivity

Once the defect formation energies have been determined, the defect concentration can be calculated. Assuming that the contributions of pressure and entropy to the Gibbs free energy can be neglected, the concentration of point defects X<sup>q</sup> at thermodynamic equilibrium is given by [57]

$$C = N_X g_X \exp\left(-\frac{E_f[X^q]}{k_B T}\right), \quad (6)$$

where  $N_X$  is the density of defects X<sup>q</sup> that can form per unit volume and  $g_X$  is the degeneracy corresponding to each charge state q. The hole concentration ( $p$ ) in the valence

band and electron concentration ( $n$ ) in the conduction band are calculated from the Fermi-Dirac distribution as

$$p = \int_{-\infty}^{\epsilon_{VBM}} D(\epsilon) \frac{1}{e^{(\epsilon_F - \epsilon)/k_B T} + 1} d\epsilon, \quad (7)$$

$$n = \int_{\epsilon_{CBM}}^{\infty} D(\epsilon) \frac{1}{e^{(\epsilon - \epsilon_F)/k_B T} + 1} d\epsilon, \quad (8)$$

where  $D(\epsilon)$  is the DOS dispersion in pristine CdPS<sub>3</sub>. Although defects have different charge states, in the absence of external charge injection, the material has to be constrained to charge neutrality,

$$p - n + \sum q C[X^q] = 0. \quad (9)$$

The method of calculating the defect density for the 2D material with a vacuum layer is given in the Supplemental Material [39]. Figure 8(a) shows the equilibrium concentration  $C$  of Cd vacancies as a function of temperature  $T$ . As expected from the defect formation energy

TABLE II. Diffusion barriers  $E_b$ , ZPE-corrected activation barriers  $E_a$ , and diffusion rates  $\Gamma$  at room temperature (300 K) for Li-ion diffusion along path I and path II as calculated by PBE, SCAN, and HSE06 functionals.

	PBE			SCAN			HSE06		
	$E_b$ (eV)	$E_a$ (eV)	$\Gamma$ (s <sup>-1</sup> )	$E_b$ (eV)	$E_a$ (eV)	$\Gamma$ (s <sup>-1</sup> )	$E_b$ (eV)	$E_a$ (eV)	$\Gamma$ (s <sup>-1</sup> )
Path I	0.248	0.235	$5.22 \times 10^8$	0.315	0.300	$4.09 \times 10^7$	0.213	0.200	$2.05 \times 10^9$
Path II	0.703	0.689	$1.29 \times 10^1$	0.793	0.778	$4.19 \times 10^{-1}$	0.789	0.775	$4.66 \times 10^{-1}$

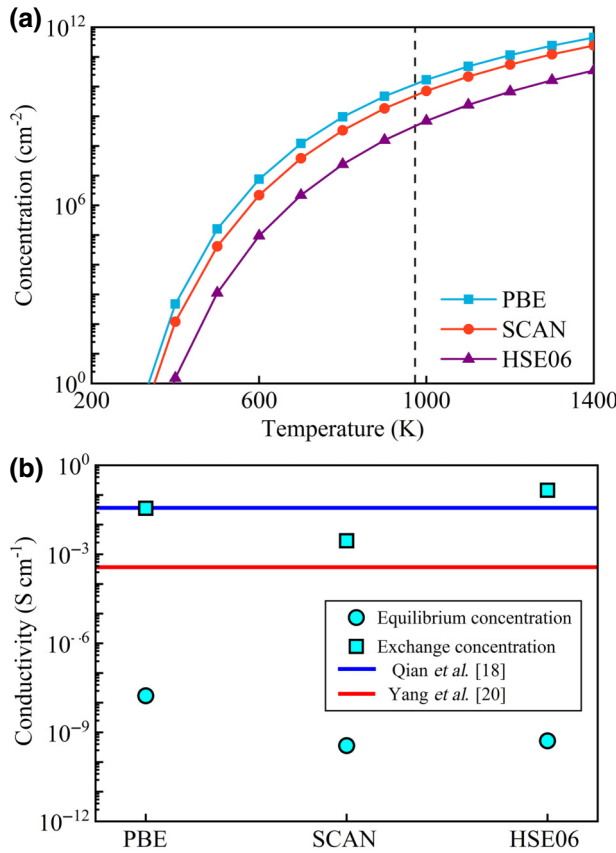


FIG. 8. (a) Cd-vacancy concentration in  $\text{CdPS}_3$  as a function of temperature  $T$  under the Cd-poor limit. The dashed line represents the annealing temperature of  $700^\circ\text{C}$  during the growth synthesis of  $\text{CdPS}_3$ , as reported in Refs. [18,20]. (b) Electrical conductivity in  $\text{Cd}_{0.833}\text{PS}_3\text{Li}_{0.333}$  ( $300 \text{ K}$ ) as calculated from Eq. (10) with equilibrium and exchange concentrations and the experimental measurements from Qian *et al.* [18] and Yang *et al.* [20].

diagrams, the dominant defect is  $V_{\text{Cd}}$ . At annealing temperature  $T = 700^\circ\text{C}$  [18,21], the 2D concentration of Cd vacancies is calculated to be  $1.24 \times 10^{10} \text{ cm}^{-2}$  (PBE),  $5.10 \times 10^9 \text{ cm}^{-2}$  (SCAN), and  $4.83 \times 10^8 \text{ cm}^{-2}$  (HSE06). There are no experimental data on the equilibrium defect concentration in 2D  $\text{CdPS}_3$ . Therefore, it is not possible to directly compare the calculated data with experimental results. We need to further calculate the Li-ion conductivity by combining existing data that can be experimentally validated.

As shown in Fig. 5(a), the Li-ion electrical conductivity in  $\text{Cd}_{1-x}\text{PS}_3\text{Li}_{2x}$  can be calculated using the Nernst-Einstein relationship [58,59],

$$\sigma_{\text{Li}} = \frac{Z^2 D C q^2}{k_B T}, \quad (10)$$

where  $Z$  is the valence of Li,  $k_B$  is the Boltzmann constant,  $D$  is the self-diffusion coefficient at temperature  $T$ ,  $C$

is the concentration of mobile Li ions,  $q = e$  is the elementary electron charge. The self-diffusion coefficient  $D$  can be estimated from the calculated diffusion rate  $\Gamma$  [Eq. (4)] and diffusion length  $L$  based on the random-walk theory [59],

$$D = \frac{1}{6} L^2 \Gamma. \quad (11)$$

Figure 8(b) then shows the Li-ion conductivities ( $300 \text{ K}$ ) obtained by substituting the Li-ion equilibrium concentration  $C$  of into Eq. (10), which ranges from  $10^{-10}$  to  $10^{-8} \text{ S cm}^{-1}$ , at least 4 orders of magnitude lower than the experimental measurements (approximately  $10^{-4}$ – $10^{-2} \text{ S cm}^{-1}$ ) [18,20]. We believe that the severe underestimation of the Li-ion conductivity is mainly due to the error in considering the Li-ion concentration. The ionic conductivity model for the  $\text{Cd}_{1-x}\text{PS}_3\text{Li}_{2x}$  monolayer is described in the Supplemental Material [39].

$\text{Cd}_{1-x}\text{PS}_3\text{Li}_{2x}$  was experimentally synthesized by Li-ion exchange in solution [18], which appears to be independent of the thermodynamic equilibrium concentration produced by annealing synthesis. Therefore, we plan to directly calculate the concentration of Li ions in the atomic structure of  $\text{Cd}_{0.833}\text{PS}_3\text{Li}_{0.333}$  (for comparison with experimentally prepared  $\text{Cd}_{0.85}\text{PS}_3\text{Li}_{0.3}$ ), referred to as the exchange concentration. We can easily determine that the 2D Li-ion concentration  $C$  in  $\text{Cd}_{0.833}\text{PS}_3\text{Li}_{0.333}$  is  $1.98 \times 10^{14} \text{ cm}^{-2}$ , and based on Eq. (10), the calculated Li-ion conductivity is in the range of  $10^{-3}$  to  $10^{-1} \text{ S cm}^{-1}$ , as shown in Fig. 8(b), which is very close to the measured experimental values. Assuming long-range thermal stability is ensured, an increase in Li-ion concentration is expected to result in a higher Li-ion conductivity being achievable by the  $\text{Cd}_{1-x}\text{PS}_3\text{Li}_{2x}$  sample. Therefore, this modeling approach is valuable for estimating ion conductivity and understanding electrical transport in ionic conductors.

#### IV. CONCLUSIONS

In this work, we have systematically investigated the electronic structure, defect formation energy, and charge transition levels of several native point vacancies in  $\text{CdPS}_3$  by first-principles calculations. Among all neutral defects, sulfur vacancies have the lowest formation energy. Meanwhile, Cd vacancies with the  $-1$  charge state have an even lower formation energy under Cd- and P-poor chemical potential conditions, especially when the Fermi energy approaches the CBM. In this case, the defect formation energy approaches zero. We then studied the structural and thermal stability and diffusivity in  $\text{Cd}_{1-x}\text{PS}_3\text{Li}_{2x}$ . In order to maintain the long-range order and low diffusion barriers, the concentration of Li-ion doping on Cd vacancies ( $x$ ) should be less than 0.5. The introduction of a high density of Li ions contributes to achieving high electrical conductivity in  $\text{Cd}_{1-x}\text{PS}_3\text{Li}_{2x}$ . Using HSE06 and the CINEB method, we obtained a Li-ion diffusion barrier of 0.2 eV in

$\text{Cd}_{0.833}\text{PS}_3\text{Li}_{0.333}$ , which was highly consistent with experimental reports of  $0.21 \pm 0.022$  eV in  $\text{Cd}_{0.85}\text{PS}_3\text{Li}_{0.3}$ . The Li ions on the surface tended to move along the Cd and S atoms rather than the P atoms. We discussed the Li-ion conductivity based on the thermodynamic equilibrium concentration in annealing synthesis and the ion exchange concentration in solution synthesis, and it is very close to the experimentally reported values. Our findings contribute to the understanding of recent experiments in achieving ultrahigh Li-ion conductivity assisted by Cd vacancies [18,20,21].

## ACKNOWLEDGMENTS

This work was supported by the National Natural Science Foundation of China (Grant No. 12174291), the National Key R&D Program of China (Grant No. 2018YFA0305800), and the China Postdoctoral Science Foundation (Grant No. 2021M702532). We thank the Core Facility of Wuhan University for providing the computational resources.

- [1] M. Lozada-Hidalgo, S. Hu, O. Marshall, A. Mishchenko, A. N. Grigorenko, R. A. W. Dryfe, B. Radha, I. V. Grigorieva, and A. K. Geim, Sieving hydrogen isotopes through two-dimensional crystals, *Science* **351**, 68 (2016).
- [2] K. Jiao, J. Xuan, Q. Du, Z. Bao, B. Xie, B. Wang, Y. Zhao, L. Fan, H. Wang, Z. Hou, S. Huo, N. P. Brandon, Y. Yin, and M. D. Guiver, Designing the next generation of proton-exchange membrane fuel cells, *Nature* **595**, 361 (2021).
- [3] X. Wu, J. J. Hong, W. Shin, L. Ma, T. Liu, X. Bi, Y. Yuan, Y. Qi, T. W. Surta, W. Huang, J. Neuefeind, T. Wu, P. A. Greaney, J. Lu, and X. Ji, Diffusion-free Grotthuss topochemistry for high-rate and long-life proton batteries, *Nat. Energy* **4**, 2 (2019).
- [4] M. Faraday, XX. Experimental researches in electricity. — fourth series, *Philos. Trans. R. Soc. London* **123**, 507 (1833).
- [5] M. Faraday, VII. Experimental researches in electricity. —twelfth series, *Philos. Trans. R. Soc. London* **128**, 83 (1838).
- [6] Q. Zhao, S. Stalin, C.-Z. Zhao, and L. A. Archer, Designing solid-state electrolytes for safe, energy-dense batteries, *Nat. Rev. Mater.* **5**, 3 (2020).
- [7] Z. W. B. Iton and K. A. See, Multivalent ion conduction in inorganic solids, *Chem. Mater.* **34**, 881 (2022).
- [8] S. Park, Y. Tulchinsky, and M. Dincă, Single-ion  $\text{Li}^+$ ,  $\text{Na}^+$ , and  $\text{Mg}^{2+}$  solid electrolytes supported by a mesoporous anionic Cu–azolate metal–organic framework, *J. Am. Chem. Soc.* **139**, 13260 (2017).
- [9] M.-T. F. Rodrigues, G. Babu, H. Gullapalli, K. Kalaga, F. N. Sayed, K. Kato, J. Joyner, and P. M. Ajayan, A materials perspective on Li-ion batteries at extreme temperatures, *Nat. Energy* **2**, 8 (2017).
- [10] S. Manzeli, D. Ovchinnikov, D. Pasquier, O. V. Yazyev, and A. Kis, 2D transition metal dichalcogenides, *Nat. Rev. Mater.* **2**, 17033 (2017).
- [11] L. Li, Y. Yu, G. J. Ye, Q. Ge, X. Ou, H. Wu, D. Feng, X. H. Chen, and Y. Zhang, Black phosphorus field-effect transistors, *Nat. Nanotechnol.* **9**, 372 (2014).
- [12] Y. Wang, J. Ying, Z. Zhou, J. Sun, T. Wen, Y. Zhou, N. Li, Q. Zhang, F. Han, Y. Xiao, P. Chow, W. Yang, V. V. Struzhkin, Y. Zhao, and H. Mao, Emergent superconductivity in an iron-based honeycomb lattice initiated by pressure-driven spin-crossover, *Nat. Commun.* **9**, 1 (2018).
- [13] S. Xue, L. Chen, Z. Liu, H.-M. Cheng, and W. Ren,  $\text{NiPS}_3$  nanosheet–graphene composites as highly efficient electrocatalysts for oxygen evolution reaction, *ACS Nano* **12**, 5297 (2018).
- [14] F. Wang, T. A. Shifa, P. He, Z. Cheng, J. Chu, Y. Liu, Z. Wang, F. Wang, Y. Wen, L. Liang, and J. He, Two-dimensional metal phosphorus trisulfide nanosheet with solar hydrogen-evolving activity, *Nano Energy* **40**, 673 (2017).
- [15] R. Samal, G. Sanyal, B. Chakraborty, and C. Sekhar Rout, Two-dimensional transition metal phosphorous trichalcogenides ( $\text{MPX}_3$ ): A review on emerging trends, current state and future perspectives, *J. Mater. Chem. A* **9**, 2560 (2021).
- [16] K. Hwangbo, Q. Zhang, Q. Jiang, Y. Wang, J. Fonseca, C. Wang, G. M. Diederich, D. R. Gamelin, D. Xiao, J.-H. Chu, W. Yao, and X. Xu, Highly anisotropic excitons and multiple phonon bound states in a van der Waals antiferromagnetic insulator, *Nat. Nanotechnol.* **16**, 6 (2021).
- [17] A. J. Martinolich, C.-W. Lee, I.-T. Lu, S. C. Bevilacqua, M. B. Peefer, M. Bernardi, A. Schleife, and K. A. See, Solid-state divalent ion conduction in  $\text{ZnPS}_3$ , *Chem. Mater.* **31**, 3652 (2019).
- [18] X. Qian, L. Chen, L. Yin, Z. Liu, S. Pei, F. Li, G. Hou, S. Chen, L. Song, K. H. Thebo, H.-M. Cheng, and W. Ren,  $\text{CdPS}_3$  nanosheets-based membrane with high proton conductivity enabled by Cd vacancies, *Science* **370**, 596 (2020).
- [19] Y. Guo, Y. Ying, Y. Mao, X. Peng, and B. Chen, Polystyrene sulfonate threaded through a metal–organic framework membrane for fast and selective lithium-ion separation, *Angew. Chem., Int. Ed.* **128**, 15344 (2016).
- [20] X. Yang, Y. Luo, J. Li, H. Wang, Y. Song, J. Li, and Z. Guo, Tuning mixed electronic/ionic conductivity of 2D  $\text{CdPS}_3$  nanosheets as an anode material by synergistic intercalation and vacancy engineering, *Adv. Funct. Mater.* **32**, 2112169 (2022).
- [21] X. Yu and W. Ren, 2D  $\text{CdPS}_3$ -based versatile superionic conductors, *Nat. Commun.* **14**, 1 (2023).
- [22] G. Henkelman, B. P. Uberuaga, and H. Jónsson, A climbing image nudged elastic band method for finding saddle points and minimum energy paths, *J. Chem. Phys.* **113**, 9901 (2000).
- [23] G. Henkelman and H. Jónsson, Improved tangent estimate in the nudged elastic band method for finding minimum energy paths and saddle points, *J. Chem. Phys.* **113**, 9978 (2000).
- [24] G. Kresse and J. Furthmüller, Efficiency of ab-initio total energy calculations for metals and semiconductors using a plane-wave basis set, *Comput. Mater. Sci.* **6**, 15 (1996).
- [25] G. Kresse and J. Furthmüller, Efficient iterative schemes for *ab initio* total-energy calculations using a plane-wave basis set, *Phys. Rev. B* **54**, 11169 (1996).

- [26] G. Kresse and J. Hafner, *Ab initio* molecular-dynamics simulation of the liquid-metal-amorphous-semiconductor transition in germanium, *Phys. Rev. B* **49**, 14251 (1994).
- [27] G. Kresse and D. Joubert, From ultrasoft pseudopotentials to the projector augmented-wave method, *Phys. Rev. B* **59**, 1758 (1999).
- [28] J. P. Perdew, K. Burke, and M. Ernzerhof, Generalized gradient approximation made simple, *Phys. Rev. Lett.* **77**, 3865 (1996).
- [29] J. Sun, A. Ruzsinszky, and J. P. Perdew, Strongly constrained and appropriately normed semilocal density functional, *Phys. Rev. Lett.* **115**, 036402 (2015).
- [30] J. Heyd, G. E. Scuseria, and M. Ernzerhof, Hybrid functionals based on a screened Coulomb potential, *J. Chem. Phys.* **118**, 8207 (2003).
- [31] H. J. Monkhorst and J. D. Pack, Special points for Brillouin-zone integrations, *Phys. Rev. B* **13**, 5188 (1976).
- [32] A. Tkatchenko and M. Scheffler, Accurate molecular van der Waals interactions from ground-state electron density and free-atom reference data, *Phys. Rev. Lett.* **102**, 073005 (2009).
- [33] H. Peng, Z.-H. Yang, J. P. Perdew, and J. Sun, Versatile van der Waals density functional based on a meta-generalized gradient approximation, *Phys. Rev. X* **6**, 041005 (2016).
- [34] G. Kresse and J. Hafner, *Ab initio* molecular dynamics for liquid metals, *Phys. Rev. B* **47**, 558 (1993).
- [35] R. Car and M. Parrinello, Unified approach for molecular dynamics and density-functional theory, *Phys. Rev. Lett.* **55**, 2471 (1985).
- [36] V. Wang, N. Xu, J.-C. Liu, G. Tang, and W.-T. Geng, VASP-KIT: A user-friendly interface facilitating high-throughput computing and analysis using VASP code, *Comput. Phys. Commun.* **267**, 108033 (2021).
- [37] K. Du, X. Wang, Y. Liu, P. Hu, M. I. B. Utama, C. K. Gan, Q. Xiong, and C. Kloc, Weak van der Waals stacking, wide-range band gap, and Raman study on ultrathin layers of metal phosphorus trichalcogenides, *ACS Nano* **10**, 1738 (2016).
- [38] D. Mukherjee, P. M. Austeria, and S. Sampath, Two-dimensional, few-layer phosphochalcogenide, FePS<sub>3</sub>: A new catalyst for electrochemical hydrogen evolution over wide pH range, *ACS Energy Lett.* **1**, 367 (2016).
- [39] Supplemental Material at <http://link.aps.org/supplemental/10.1103/PhysRevApplied.21.044011> for the calculations of defect formation energy; structural parameters of secondary compounds; the PBE and SCAN band structures with SOC; the membranes under AIMD simulations; the Li-ion diffusion paths, energy profiles, rates, concentrations, and conductivity.
- [40] D. I. Bilc, R. Orlando, R. Shaltaf, G.-M. Rignanese, J. Íñiguez, and Ph. Ghosez, Hybrid exchange-correlation functional for accurate prediction of the electronic and structural properties of ferroelectric oxides, *Phys. Rev. B* **77**, 165107 (2008).
- [41] F. Boucher, M. Evain, and R. Brec, Second-order Jahn—Teller Effect in CdPS<sub>3</sub> and ZnPS<sub>3</sub> demonstrated by a non-harmonic behaviour of Cd<sup>2+</sup> and Zn<sup>2+</sup>D<sup>10</sup> ions, *J. Alloys Compd.* **215**, 63 (1994).
- [42] C. Calareso, V. Grasso, and L. Silipigni, Optical spectra of the layered Cd<sub>2</sub>P<sub>2</sub>S<sub>6</sub> and Cd<sub>2</sub>P<sub>2</sub>Se<sub>6</sub> compounds in the region from 1.6 to 5.5 eV, *J. Appl. Phys.* **82**, 6228 (1997).
- [43] R. Ramprasad, H. Zhu, P. Rinke, and M. Scheffler, New perspective on formation energies and energy levels of point defects in nonmetals, *Phys. Rev. Lett.* **108**, 066404 (2012).
- [44] C. Freysoldt, B. Grabowski, T. Hickel, J. Neugebauer, G. Kresse, A. Janotti, and C. G. Van de Walle, First-principles calculations for point defects in solids, *Rev. Mod. Phys.* **86**, 253 (2014).
- [45] C. Freysoldt and J. Neugebauer, First-principles calculations for charged defects at surfaces, interfaces, and two-dimensional materials in the presence of electric fields, *Phys. Rev. B* **97**, 205425 (2018).
- [46] C. Freysoldt, J. Neugebauer, and C. G. Van de Walle, Fully *ab initio* finite-size corrections for charged-defect supercell calculations, *Phys. Rev. Lett.* **102**, 016402 (2009).
- [47] C. Freysoldt, J. Neugebauer, and C. G. Van de Walle, Electrostatic interactions between charged defects in supercells, *Phys. Status Solidi B* **248**, 1067 (2011).
- [48] B. Rijal, A. M. Z. Tan, C. Freysoldt, and R. G. Hennig, Charged vacancy defects in monolayer phosphorene, *Phys. Rev. Mater.* **5**, 124004 (2021).
- [49] A. M. Z. Tan, M. A. Garcia, and R. G. Hennig, Giant Stokes shift for charged vacancies in monolayer SnS, *Phys. Rev. Mater.* **6**, 044003 (2022).
- [50] G. Makov and M. C. Payne, Periodic boundary conditions in *ab initio* calculations, *Phys. Rev. B* **51**, 4014 (1995).
- [51] S. Lany and A. Zunger, Accurate prediction of defect properties in density functional supercell calculations, *Modell. Simul. Mater. Sci. Eng.* **17**, 084002 (2009).
- [52] M. Ohwada, K. Kimoto, T. Mizoguchi, Y. Ebina, and T. Sasaki, Atomic structure of titania nanosheet with vacancies, *Sci. Rep.* **3**, 2801 (2013).
- [53] W.-J. Yin, Y. Yan, and S.-H. Wei, Anomalous alloy properties in mixed halide perovskites, *J. Phys. Chem. Lett.* **5**, 3625 (2014).
- [54] M. Xu, M. S. Park, J. M. Lee, T. Y. Kim, Y. S. Park, and E. Ma, Mechanisms of Li<sup>+</sup> transport in garnet-type cubic Li<sub>3+x</sub>La<sub>3</sub>M<sub>2</sub>O<sub>12</sub> (*M* = Te, Nb, Zr), *Phys. Rev. B* **85**, 052301 (2012).
- [55] W. Tang, E. Sanville, and G. Henkelman, A grid-based Bader analysis algorithm without lattice bias, *J. Phys.: Condens. Matter* **21**, 084204 (2009).
- [56] L. F. Huang, M. Y. Ni, X. H. Zheng, W. H. Zhou, Y. G. Li, and Z. Zeng, Ab initio simulations of the kinetic properties of the hydrogen monomer on graphene, *J. Phys. Chem. C* **114**, 22636 (2010).
- [57] J. Buckeridge, Equilibrium point defect and charge carrier concentrations in a material determined through calculation of the self-consistent Fermi energy, *Comput. Phys. Commun.* **244**, 329 (2019).
- [58] D. J. Evans and G. P. Morriss, *Statistical Mechanics of Nonequilibrium Liquids* (ANU Press, Canberra, 2007).
- [59] C. Kofahl, L. Dörrer, B. Muscutt, S. Sanna, S. Hurskyy, U. Yakhnevych, Y. Suhak, H. Fritze, S. Ganschow, and H. Schmidt, Li self-diffusion and ion conductivity in congruent LiNbO<sub>3</sub> and LiTaO<sub>3</sub> single crystals, *Phys. Rev. Mater.* **7**, 033403 (2023).